Int J Adv Manuf Technol (2009) 45:300–317
DOI 10.1007/s00170-009-1972-4

ORIGINAL ARTICLE

Development of an intelligent process model for EDM

S. N. Joshi · S. S. Pande

Received: 23 April 2008 / Accepted: 10 February 2009 / Published online: 14 March 2009

Abstract This paper reports the development of an intelligent model for the electric discharge machining (EDM) process using finite-element method (FEM) and artificial neural network (ANN). A two-dimensional axi-symmetric thermal (FEM) model of single-spark EDM process has been developed based on more realistic assumptions such as Gaussian distribution of heat flux, time- and energy-dependent spark radius, etc. to predict the shape of crater cavity, material removal rate, and tool wear rate. The model is validated using the reported analytical and experimental results. A neural-network-based process model is proposed to establish relation between input process conditions (discharge power, spark on time, and duty factor) and the process responses (crater geometry, material removal rate, and tool wear rate) for various work—tool work materials. The ANN model was trained, tested, and tuned using the data generated from the numerical (FEM) simulations. The ANN model was found to accurately predict EDM process responses for chosen process conditions. It can be used for the selection of optimum process conditions for EDM process.

Keywords Electric discharge machining (EDM) · Process modeling and simulation · Finite-element method (FEM) · Backpropagation neural networks (BPNN)

Nomenclature

C_p	workpiece-specific heat (J/kg K)
F_a	fraction of power going to the anode
F_c	fraction of power going to the cathode
I	discharge current (A)
K_t	workpiece thermal conductivity (W/m K)
MRR	material removal rate (mm^3/min)
q_w	heat flux at cathode surface (W/m^2)
r	radial coordinate
R_{pc}	spark radius at cathode surface (μm)
t	time (s)
T	temperature (K)
T_a	ambient temperature (K)
T_m	melting temperature (K)
T_d	spark on time (μs)
TWR	tool wear rate (mm^3/min)
V	discharge voltage (V)
x	input variable
x_{max}	maximum value of input variable
x_n	normalized value of input variable
z	depth or axial coordinate
ρ	workpiece density (kg/m^2)

1 Introduction

Electric discharge machining (EDM) is a nontraditional manufacturing process that uses electric spark discharges to machine electrically conductive materials. In today's manufacturing scenario, EDM contributes a prime share in the manufacture of complex-shaped dies, molds, and critical parts used in automobile, aerospace, and other industrial applications [1]. It is, thus, important to improve the process productivity and finishing capability to produce complex part shapes accurately in the shortest possible lead times.

S. N. Joshi · S. S. Pande (✉)
Computer-Aided Manufacturing Laboratory, Department of Mechanical Engineering, Indian Institute of Technology Bombay, Mumbai 400076, India
e-mail: s.s.pande@iitb.ac.in

During the EDM process, discharge phenomenon occurs over a very short period of a few microseconds in a narrow space filled with dielectric fluid. Occurrence of spark causes evaporation and melting of the material from both the electrodes. Owing to the complex nature of the process involving physics of the EDM spark (plasma), it is difficult to observe the process experimentally and quantify the mechanism of material removal [2]. Researchers worldwide are thus focusing their attention on developing EDM process models for accurate prediction of crater shapes, material removal rate (MRR), and tool wear rate (TWR). Literature reports extensive studies on various aspects of EDM process such as different machine types (wire cut/die sinking), tooling, control circuits, selection of process conditions based on experimental analysis, online machine control, and studies on the microstructure of the machined workpiece [3, 4]. These studies are, however, applicable to specific tool–work materials, machines, and shop conditions. The key issues in die-sinking EDM process include economical machining and accurate reproduction of complex tool shape into the die cavity. The focus of the present work is on developing an intelligent process model for EDM for accurate prediction of crater cavity, MRR, and TWR using finite-element method (FEM) and artificial neural network (ANN). This model will help in the selection of optimum process parameters to improve the process productivity and finishing capability during application.

The rest of the paper is organized as follows. "Section 2" presents a review of relevant papers on the numerical analysis of single-spark EDM process and the use of ANN for process modeling. Overview of the developed integrated process model for EDM using FEM and ANN is presented in "Section 3." "Section 4" describes, in details, the thermal analysis of EDM process using FEM while in "Section 5" the influence of various input process parameters on process performance parameters is discussed. Development of ANN-based process model is presented in "Section 6." "Section 7" summarizes the conclusions and contributions from this work.

2 Literature review

Since early 1970s, researchers worldwide have attempted mathematical modeling of EDM process (plasma channel) to understand the electric discharge phenomena and the mechanism of cathode and anode erosion. Two different mechanisms have been reported to analyze the material removal in EDM process viz. electromechanical analysis [5] and electrothermal analysis [6–18]; the former mechanism being applicable for short pulses typically less than 5 μs. Material removal in EDM process is primarily due to the intense heat generated by a plasma arc produced between the cathode and the anode. As a result, the electrothermal analysis of EDM process is considered more relevant in the present context.

Literature reports various two-dimensional heat flow models of EDM process considering semifinite [6, 10–14] or infinite [8] cylindrical electrodes. Several assumptions such as cylindrical spark plasma [6–14], uniform (disk) heat source [6, 8, 10–13], distributed point heat source [9], constant [6, 8, 12, 14] or expanding heat flux radius [7, 13, 15], and constant thermophysical properties [6, 8, 10–13] over temperature range were employed. These simplifying assumptions severely limit the applicability of the results.

In late 1980s, DiBitonto and co-workers developed a point heat source model [16] for cathode erosion and disk-shaped heat source model with Gaussian distribution of heat flux for anode [17], considering average thermophysical properties. The spark radius for anode was approximated based on the results of underwater welding experiments.

Salah et al. [18] developed a steady-state heat diffusion model considering Gaussian-distributed heat source and reported that consideration of temperature-dependent thermal conductivity is important in the thermal analysis of EDM process. Marafona and Chousal [19] developed an electrothermal model based on Joule effect using FEM. The resulting melting volume per discharge pulse was compared with experimental data reported by DiBitonto et al. [16].

Recently, Yeo et al. [20] critically compared various EDM thermal models reported by Beck [10, 11], DiBitonto et al. [16], Jilani and Pandey [12, 13], Snoyes and Van Dijck [6], and Van Dijck and Dutre [8] with the experimental results (AGIE SIT data) published by DiBitonto et al. [16] in terms of the predicted geometry of the crater due to single spark and material removal at the cathode. It has been reported that DiBitonto's model predicts results closer to the experimental data as compared to all the other models which overpredict significantly. However, DiBitonto's process model has limited applicability due to simplifying assumptions such as the approximation of heat source at cathode as a point and crater cavity of hemispherical shape, which is not realistic.

In general, it can be concluded that the reported theoretical models based on thermal analysis have limited applicability, as they are based on the assumptions like the use of constant spark radius, approximation of heat source to a point, or disk-shaped (uniform) and constant thermal properties of work–tool materials. A need thus exists to develop a more comprehensive numerical model based on thermal analysis of EDM spark to predict accurately the crater cavity by modifying above-stated assumptions.

Literature shows few attempts in using ANN for modeling of EDM process. Tsai and Wang [21] have used six different network configurations and have reported that training and testing by using adaptive-network-based fuzzy inference system provides better accuracy compared with other configurations. Wang et al. [22] and Su et al. [23] have developed a hybrid approach for modeling and optimization of EDM process using ANN and genetic algorithm (GA) to obtain process parameters for optimal performances such as MRR and surface roughness. Amalnik and Farzad [24] reported the use of backpropagation neural network (BPNN) and radial basis function network (RBFN) for prediction of EDM process parameters (MRR and TWR). Panda and Bhoi [25] used Levenberg–Marquardt backpropagation technique to predict the MRR. Mandal et al. [26] have used BPNN based on the experimental data and further optimized the process parameters using nonsorting GA.

Most of the above-reported ANN models have been trained based on the experimental data obtained on specific machines for typical work–tool materials. Scant research work is reported on accurate prediction of crater shapes and surface roughness during the finish machining of complex dies/mold cavities using EDM process.

A need exists to develop an intelligent process model of the EDM process considering thermophysical characteristics to accurately predict crater shapes, MRR, and TWR for a variety of work–tool materials and EDM process conditions. The present work is an attempt towards the development of such integrated EDM process model using FEM and ANN.

3 Integrated process model development

Figure 1 shows the overall methodology for the development of integrated process model of EDM. It is primarily comprised of two stages, viz. numerical (FEM) analysis of the EDM process considering the thermophysical characteristics of the process and the development of ANN-based process model based on the data generated using numerical (FEM) simulations. This approach of model development has a peculiar merit that it is based on the accurate finite-element analysis and not on experimental data collection, which could be costly, time consuming, and error prone.

Various steps in the development of process model are discussed in the sections to follow.

4 Numerical modeling of the EDM process

4.1 The EDM process

In EDM process, a controlled spark is generated between two metal electrodes (tool and the workpiece) immersed in a dielectric medium which are separated from each other with a small gap usually of the order of 10 µm [27]. DC voltage (80–200 V) is applied between the tool and the workpiece. For coarse machining operations, the tool is usually the anode and the workpiece is the cathode, while the polarities are reversed for fine machining operations. Controlled pulsing of direct current between the tool and the workpiece produces spark discharges forming a plasma channel between the cathode and anode. The spark occurs at the spot where the tool and the workpiece surface are closest. During the on time of EDM pulse (of the order of microsecond), intense heat is generated which causes melting and vaporization of the metal. Due to the large amount of plasma pressure (3 kbar) [16], the molten metal holds back at its place. As soon as the spark duration time is over, the spark collapses and the dielectric gushes in to fill the void. This sudden removal of pressure results in a violent ejection of the molten metal from the work surface resulting in the formation of small craters on the surface. Owing to the complex nature of the process involving spark plasma, dielectric medium, flushing conditions, etc., it is difficult to carry out the experimental observations.

4.2 Thermal analysis of the EDM process

During the process, high electric potential applied between cathode and anode ionizes the dielectric medium producing a plasma arc. The primary mechanism of material removal

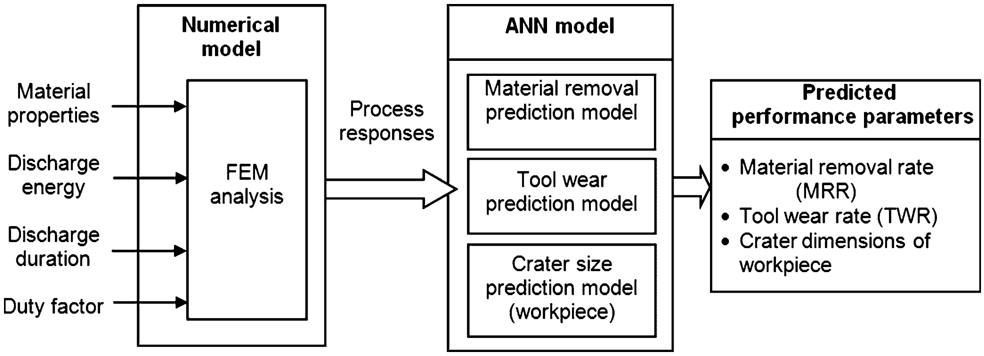

Fig. 1 Integrated process model development

in EDM process is the thermal heating of work surface due to intense heat generated by the plasma. The highly charged ionized particles of the plasma raise the temperature of the electrodes (tool, work) beyond their melting point, sometimes even more than that of boiling point. For the thermal analysis of the process, conduction is thus considered as the primary mode of heat transfer between the ions of plasma and the molecules of work–tool [6–9].

In the present work, Fourier heat conduction equation with necessary boundary conditions is taken as the governing equation. Transient nonlinear analysis of the single-spark operation of EDM process has been carried out. During the process, spark discharges may occur over work surface at locations where the interelectrode gap is minimum. All discharges can be considered to be identical. The present analysis is thus carried out for a single-spark operation. A small cylindrical portion of the workpiece around the spark is chosen for analysis. Figures 2 and 3 show the two-dimensional axisymmetric process continuum and the associated boundary conditions.

The following assumptions have been made during the thermal analysis.

4.2.1 Assumptions

- Workpiece and tool materials are homogeneous and isotropic in nature.
- The material properties of the workpiece and tool are temperature dependent.
- Heat transfer is purely by conduction. Radiation and convection heat losses are neglected.
- EDM spark channel is considered as a cylindrical column.
- The spark radius is assumed to be a function of discharge current and time.
- Flushing efficiency is considered to be 100%. There is no deposition of recast layer on the machined surfaces.

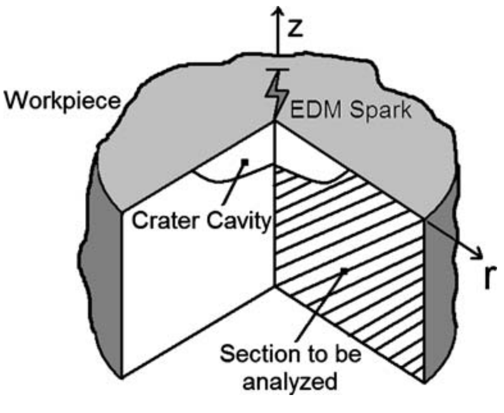

Fig. 2 Schematic of process continuum

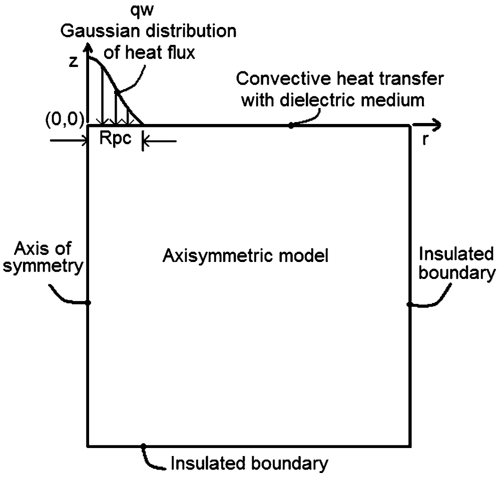

Fig. 3 Boundary conditions for solution

- Only a fraction of total spark energy is dissipated as heat into the workpiece; the rest is lost into the dielectric convection and radiation.
- Heat flux is assumed to be Gaussian-distributed. The zone of influence of the spark is assumed to be axisymmetric in nature.

4.2.2 Governing equation

For the thermal analysis of EDM process, Fourier heat conduction equation is taken as the governing equation

$$\frac{1}{r}\frac{\partial}{\partial r}\left(K_{\mathrm{t}} r \frac{\partial T}{\partial r}\right)+\frac{\partial}{\partial z}\left(K_{\mathrm{t}}\frac{\partial T}{\partial z}\right)=\rho C_{\mathrm{p}}\frac{\partial T}{\partial t} \tag{1}$$

where r and z are the coordinates of cylindrical work domain; T is temperature; K_{t} is thermal conductivity; ρ is density; C_{p} is specific heat capacity of workpiece material.

4.2.3 Boundary conditions

Figure 3 shows the associated boundary conditions applied. In EDM process, the workpiece is immersed in dielectric medium; the temperature of the domain is thus assumed to be ambient temperature (T_{a}) to start with. The boundaries of the domain away from the spark domain are considered as insulated. Heat flux (q_{w}) boundary condition is applied on the top surface of the workpiece where the spark occurs.

4.2.4 Heat input

Important factors which contribute to the accurate calculation of material removal rate in single-spark EDM model include the amount of heat input, radius of plasma spark, and thermophysical properties of material. Researchers have assumed two forms of heat input models, viz. point source model with hemispherical crater cavity [16] or uniformly distributed heat flux model [6–13]. Both these are simplistic as in actual practice neither is there a point source (like laser beam) nor is there any uniform (constant) application of heat on the workpiece. A spark radius exists at the cathode electrode [2]. Consideration of average thermophysical material properties and constant EDM spark radius make the reported models [6–13] simplistic and restrict their further applicability.

In this present work, the Gaussian distribution of heat input proposed by Patel et al. [17] has been used to approximate the heat from the plasma. The heat q_w entering the workpiece due to EDM spark is represented by

$$q_w(r) = q_o \exp\left\{-4.5\left(\frac{r}{R_{pc}}\right)^2\right\} \tag{2}$$

Using this equation, the maximum heat flux q_o can be calculated [28] as below.

$$q_o = \frac{4.56 F_c V I}{\pi R_{pc}^2} \tag{3}$$

Where F_c is the fraction of total EDM spark power going to the cathode; V is discharge voltage (V); I is discharge current (A); R_{pc} is spark radius (µm) at the work surface.

4.2.5 Spark radius

Spark radius is an important factor in the modeling of EDM process. In practice, it is extremely difficult to experimentally measure spark radius due to very short pulse duration of the order of few microseconds [2]. Different approaches have been proposed by researchers in the literature.

Erden [29] have proposed an empirical equation to calculate the radius in EDM process, as a function of discharge power and time. These equations are applicable for a specific pair of work and tool material and need empirical constants which are difficult to estimate.

DiBitonto et al. [16] approximated spark as a point for cathode erosion and calculated the plasma radius at anode erosion [17], which is a function of time. The empirical constants used for calculation of spark radius were based on the experimental results of underwater welding.

Pandey and Jilani [15] proposed an approach to calculate the discharge radius in the EDM process based on the boiling point temperature of work material, energy density, and the thermal diffusivity of work material. It is developed for steel and copper pair and has limited applicability. Shankar et al. [30] empirically determined the spark radius as a function of current.

The EDM spark is controlled by discharge energy and spark on time [2]. Ikai and Hashiguchi [31] have derived a semiempirical equation of spark radius namely “equivalent heat input radius” as a function of discharge current (I) and spark on time (T_d), which is more realistic as compared to other approaches.

$$R_{pc} = (2.04e-3) I^{0.43} T_d^{0.44} \tag{4}$$

In the present work, this approach has been used to calculate equivalent heat input at cathode/anode using Eqs. 2, 3, and 4. The heat flux equation derived and used for further analysis in this work is

$$q_w(t) = \frac{3.4878 \times 10^5 F_c V I^{0.14}}{T_d^{0.88}} \exp\left\{-4.5\left(\frac{t}{T_d}\right)^{0.88}\right\} \tag{5}$$

where T_d is time at the end of electric discharge (µs).

4.2.6 Energy distribution

Energy distribution is another important factor in the thermal analysis of EDM process. The total spark power gets divided into three parts, a portion conducted away by the cathode, portion conducted away by the anode, and the rest being dissipated in the dielectric. Few experimental studies have been reported in literature to determine these fractions of heat.

Shankar et al. [30] proposed that 40–45% of the heat input is absorbed by the workpiece made of 5 Cr die steel, which is calculated based on an empirical analysis using water as the dielectric and copper as the tool electrode. However, further research on spark energy distribution suggested that about 50–60% of the total heat generated during spark discharge dissipates into the cathode and anode and the rest is being dissipated into the dielectric medium through convection and radiation [32].

DiBitonto and co-workers [16, 17] used the data that were gathered over a long period of time and for different operating conditions. Comparing experimental and analytical results, it has been recommended that the energy distribution should be chosen as 18.3% for cathode (F_c) and 8±1% for anode (F_a) for good correlation between analytical and experimental results. In the present work, the same values of F_c and F_a have been chosen.

4.3 Solution methodology

The governing equation (Eq. 1) with boundary conditions outlined earlier was solved by FEM to predict the temperature distribution at the end of each transient heat transfer analysis cycle. ANSYS™ 10.0, an FEM solver was used. A 2-D continuum of size 0.5×0.5 mm was considered for the analysis. Four-noded, axisymmetric, thermal solid element (PLANE 55) was used for discretization of the continuum. Nonlinear material properties, viz. temperature-dependent thermal conductivity, were employed. Convergence conditions were tested by increasing the number of elements in the mesh. ANSYS Parametric Design Language [33] was used to build the single-spark EDM model and to automate the problem-solving process for different input process parameters.

Important steps are as follows:

- Create model geometry and mesh it using PLANE 55 thermal solid element. Refine the mesh at the location where heat flux is applied.
- Apply the material properties of work–tool materials, viz. temperature-dependent thermal conductivity, density, and heat capacity. Set initial and bulk temperature as 300 K. Apply the heat flux at the spark location (Eq. 5).
- Compute the temperature distribution for spark on time (T_d).
- Identify the nodes showing temperature more than the melting point of work material and eliminate them from the mesh.
- Calculate the MRR and TWR using coordinate data of the craters of work and tool material and the duty factor.

Figure 4 shows the temperature distribution obtained for a typical machining condition. Figure 5 shows the bowl-shaped crater cavity predicted by our model.

4.4 Model validation and results

The thermal model discussed above calculates performance parameters considering the occurrence of a single spark. Actual material removal realizable during EDM process is governed by various factors such as ignition delays, high frequency of sparks, flushing efficiency, phase change of electrodes, dielectric medium, and random behavior of debris particles. It is very difficult to incorporate these factors into the process models. In the present work, ideal material removal rates were computed for chosen process conditions (Table 1) considering that all sparks are equally effective with 100% dielectric flushing efficiency.

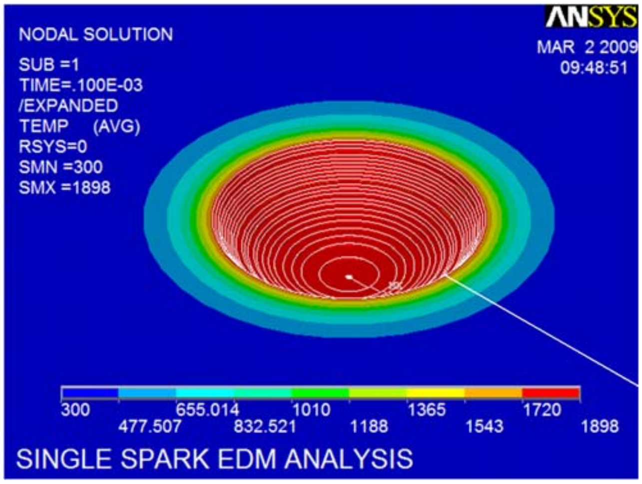

Fig. 5 Predicted bowl-shaped crater cavity using FEM analysis. (crater depth 30.2 µm, crater radius 70.3 µm, work material AISI W1 tool steel, discharge current 10 A, spark on time 100 µs, and discharge voltage 40 V)

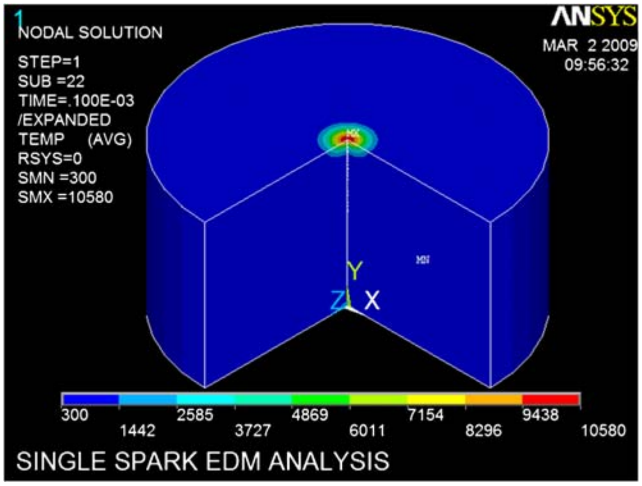

Fig. 4 Temperature distribution obtained at the end of a spark. (machining condition: work material AISI W1 tool steel, current 10 A, spark on time 100 µs, and discharge voltage 40 V)

Recently, Yeo et al. [20] critically compared the prediction accuracies of five thermal models reported by Snoyes and Van Dijck [6, 7], Van Dijck and Dutre [8], Beck [10, 11], Jilani and Pandey [12, 13], and DiBitonto et al. [16] with the experimental data [16]. It was concluded that results predicted by DiBitonto's model are closer to the experimental data compared to all the other models. It was, therefore, decided to compare the results predicted by our model with the theoretical and experimental results (AGIE SIT data) reported by Yeo et al. [20]. The machining conditions taken for carrying out our analysis were exactly the same as those reported by Yeo et al. [20]. Table 1 shows the comparison of the reported experimental results (AGIE SIT), reported theoretical model results [16, 20], and the results predicted by our model.

Figure 6 shows the comparison of MRR predicted by our model, Yeo's recommended model, and the AGIE SIT experimental data. It is seen that the values of MRR predicted by our model are further closer to the experimental results compared to those by Yeo et al. [20] for a wide range of discharge energy levels up to 650 mJ. It can, thus, be concluded that our numerical model would give better prediction of MRR compared to the reported models. This may be due to the incorporation of more accurate and realistic equivalent spark radius equation, which is a function of current and discharge duration. In addition, our model considers the transient analysis of single spark with the expanding radius, which may also add more accuracy to our results.

Table 1 Comparison of the predicted results

No.	Machining conditions				MRR (mm^3/min)		
	Current (A)	Pulse on time (µs)	Pulse off time (µs)	Discharge power (mJ)	Expt. analysis (DiBitonto et al. [16])	Theoretical analysis (DiBitonto et al. [16])	Our model
1	2.34	5.6	1	0.33	0.3	13.82	12.13
2	2.83	7.5	1.3	0.53	1.6	17.26	16.36
3	3.67	13	2.4	1.19	3.1	21.78	20.37
4	5.3	18	2.4	2.39	8.4	35.58	34.49
5	8.5	24	2.4	5.1	23.2	63.79	62.86
6	10	32	2.4	8	32	77.18	76.37
7	12.8	42	3.2	13.44	50.5	100.33	96.68
8	20	56	3.2	28	89.7	164.65	152.81
9	25	100	4.2	62.5	125	207.2	197.92
10	36	180	4.2	162	226	304.56	262.28
11	44	240	5.6	264	246	373.09	302.6
12	58	420	7.5	609	346	494.03	356.6
13	68	560	10	952	559	579.47	364.82

Work material—steel (iron), discharge voltage=25 V, thermal conductivity (K_t)=56.1 W/m K, heat capacity (C_p)=575 J/kg K, density (ρ)= 7,545 kg/m^3 , melting point temperature (T_m)=1,808 K

In comparison, Yeo's recommended model [16, 20] approximated the spark as point on cathode with created hemispherical crater cavity (see Fig. 7), which is quite simplified compared to reality.

Figure 6 shows that, for higher values of discharge power and discharge duration (discharge energy 952 mJ), our model underpredicts the MRR compared to the experimental results. This may be due to the fact that longer pulses with higher values of current provide more surface area to heat conduction, which might lead to reduction in heat density. Constant value of duty factor may also result in comparatively less MRR.

Yeo's recommended model predicts the shape of the crater cavity to be hemispherical. In comparison, our model predicts the shape of crater cavity as shallow-bowl-shaped (see Figs. 5 and 7). Similar-shaped (bowl) crater cavities have been experimentally observed by Das et al. [27], Dong [34], and Schulze et al. [35] under different EDM process conditions.

From the above comparisons, it was concluded that our model can predict the process performance parameters (MRR, shape of crater cavity) better and closer to the experimental results. It will give consistent results compared to the experimental data. As a result, it was proposed

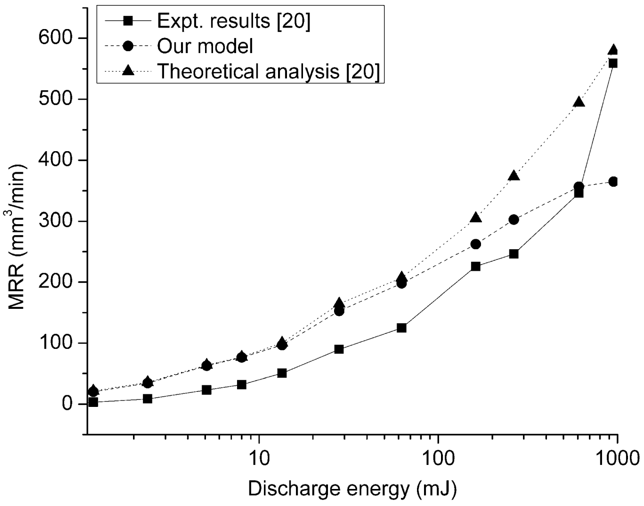

Fig. 6 Comparison of computed and experimental results

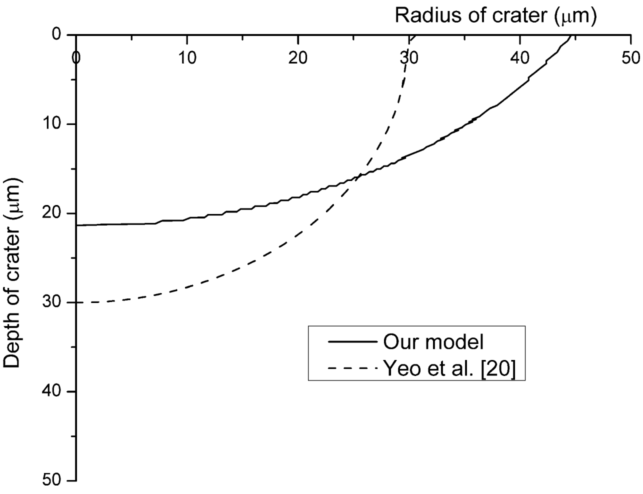

Fig. 7 Comparison of predicted crater shapes

to carry out parametric studies on our EDM process model to study the effect of various input process parameters on performance parameters with a view to develop an ANN-based intelligent process model.

5 Parametric studies on EDM process

Parametric studies were carried out by the numerical simulations using the EDM process model developed ("Section 4"). The aim was to understand the influence of input process parameters (discharge current, spark on time, discharge voltage, and duty factor) on the process performance measures such as MRR, TWR, and surface roughness (crater depth). The generated data from these numerical simulations were used for the development of ANN-based EDM process model.

The following ranges of the input process parameters identified from the published research [1, 3, 16–26, 31] and machining handbook [43] were chosen for our study.

- Discharge current: 5–10–20–30–40 A
- Discharge duration: 25–50–100–300–500–700 µs
- Duty factor: 50–65–80%
- Breakdown voltage: 30–40–50 V
- Work materials: AISI W1 tool steel, AISI P20 mold steel
- Tool materials: graphite, copper

One hundred eighty numerical simulations (90 for each work–tool material pair) were carried out in all for the range of input process parameters outlined above. Based on the temperature distribution resulting due to the single spark, MRR, TWR, and crater sizes were computed. Material properties of AISI W1 tool steel and graphite (Tables 2 and 3) were used. Table 4 shows representative results for a typical work–tool material pair (AISI W1 tool steel and graphite).

Table 2 Material properties of AISI W1 tool steel [36]

Temperature (T) K	Thermal conductivity (K_t) W/m K
323	45.19
373	48.3
533	41.5
673	38.1
813	34.6
948	29.4
1,088	24.2
1,188	24.2
1,288	24.2

Composition: C 1.0%, Mn 0.35%, Si 0.3%, Cr 0.15%; heat capacity C_p=461 J/kg K, density ρ=7,830 kg/m^3, melting point T_m=1,708 K

Table 3 Material properties of graphite [36]

Temperature (T) K	Thermal conductivity (K_t) W/mK
300	91.3
400	90.2
500	84.6
600	78
700	71.7
800	65.9
900	60.9
1,000	56.5
1,200	49.48
1,300	49.48
1,400	49.48

Heat capacity C_p=715 J/kg K, density ρ=2,190 kg/m^3, melting point T_m=3,948 K

Effects of important process parameters (discharge current, discharge voltage, spark on time, duty factor) on the performance parameters (MRR, TWR, crater depth) were studied. These are discussed in the following sections.

5.1 Effect of discharge current

Discharge current is one of the important process parameters in EDM as it directly governs the spark energy. Figure 8 shows that MRR increases monotonically with increase in discharge current and duty factor. These trends match with the experimental results reported by Chen and Mahdivian [37]. Higher values of discharge current and duty factor are recommended for rough machining, while lower values are recommended for finishing operations.

Figure 9 shows that, at higher values of discharge current, the tool electrode erodes faster affecting the cost and productivity of the EDM process.

Figure 10 shows that the crater depth (surface roughness) increases with the discharge current and voltage. It is observed that, in the low discharge current range, the crater depth increases rapidly with current but tapers off further, indicating the production of shallow and wider craters at high currents. The trend of variation of crater depth with current is also seen in the reported experimental results [38]. Lesser values of discharge currents and voltages are recommended for finishing applications of EDM process to limit the depth of the craters.

5.2 Effect of duty factor

Duty factor is defined as the ratio of spark on time to the total spark time. It governs the generation of number of sparks per unit time; higher duty factor indicates more

Table 4 Numerical simulation (FEM) results

Sr. no.	Process parameters				Performance parameters			
	Current (A)	Spark on time (µs)	Discharge voltage (V)	Duty factor (%)	MRR (mm^3/min)	TWR (mm^3/min)	Crater depth–work material (µm)	Crater radius –work material (µm)
1	5	25	30	50	36.4	0	17.3	30.4
2	5	25	40	50	50.4	2.23	20.4	31.7
3	5	25	50	50	62.2	6.23	22	34.4
4	5	50	30	50	33.8	0	20.4	37.6
5	10	50	40	50	103.8	6.44	29.9	54.8
6	10	50	50	50	126.6	15.72	33.1	57.8
7	10	100	30	50	72	0	31.5	64.6
8	10	100	40	50	101.1	0.65	36.2	70.3
9	20	100	30	50	159	1.56	38	89.2
10	20	100	40	50	212.7	7.71	42.8	95.5
11	20	100	50	50	258.3	22.1	46	100
12	20	300	30	50	141	0	50.8	126
13	30	300	40	50	328	2.72	65.4	168
14	30	300	50	50	414	21.59	73.3	179
15	30	500	40	50	319.2	0	76.5	196
16	30	500	50	50	418.2	4.27	86	211
17	40	500	50	50	548.4	18.36	86	238
18	40	700	30	50	273.4	0	71.7	222
19	40	700	40	50	413.6	0	86	247
20	40	700	50	50	552.9	4.29	100.3	266

Work material (cathode), AISI W1 tool steel; tool material (anode), graphite

number of sparks per unit time. Figures 8 and 9 show that increase in duty factor monotonically increases MRR and TWR. Higher values of duty factor can be used for roughing application at the expense of more tool erosion.

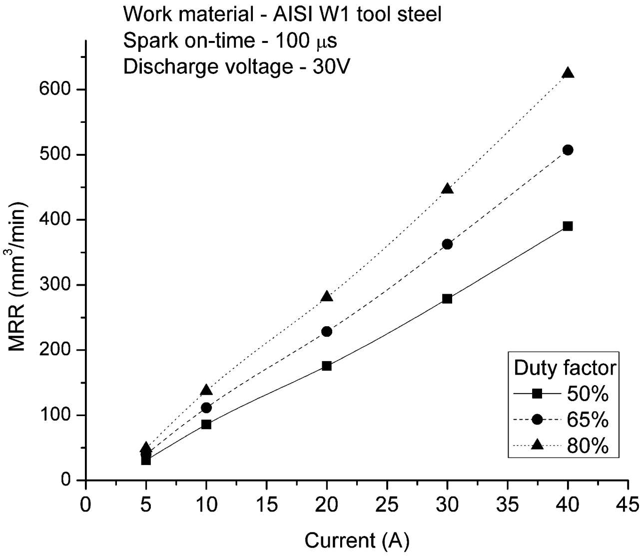

Fig. 8 Variation of MRR with discharge current

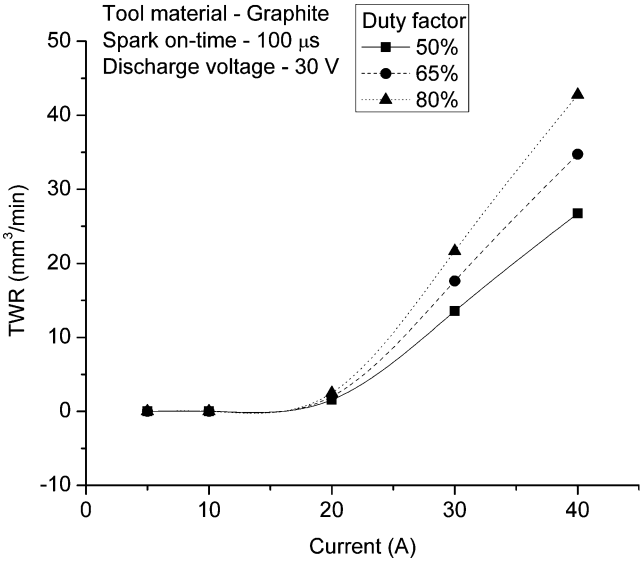

Fig. 9 Variation of TWR with discharge current

5.3 Effect of spark on time (discharge duration)

Spark discharge duration is another important process parameter in EDM, which decides the time for the

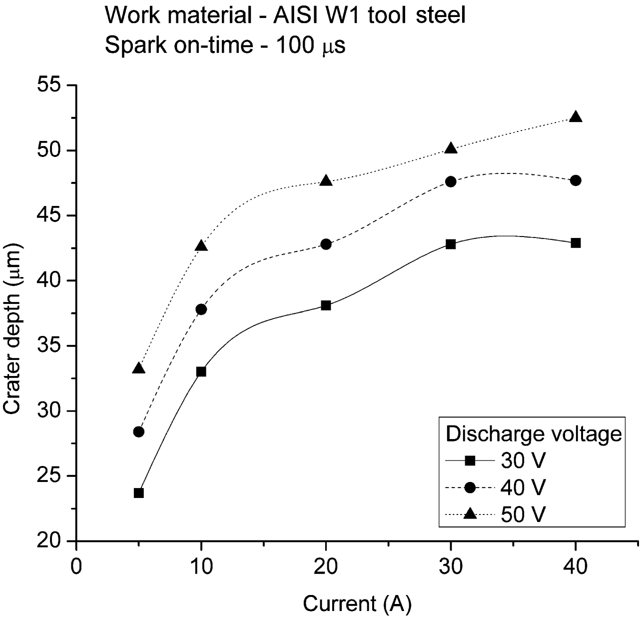

Fig. 10 Variation of crater depth with discharge current

discharge energy to be applied on the work surface during the total spark time (on+off). The spark off time is generally decided by the "duty factor".

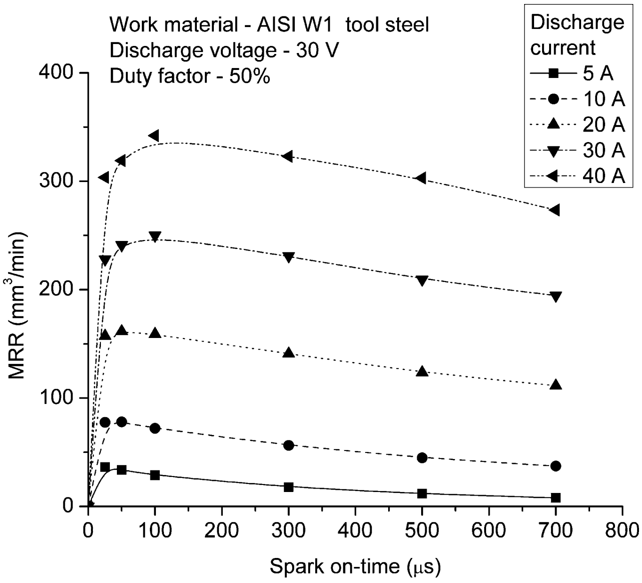

Fig. 11 Variation of MRR with spark on time

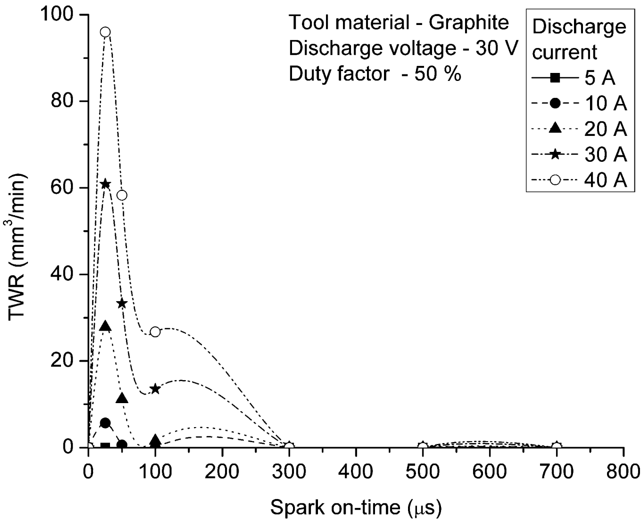

Fig. 12 Variation of TWR with spark on time

Figure 11 shows the variation of MRR with spark on time for a typical machining condition for AISI W1 tool steel and graphite work–tool pair. The amount of MRR initially increases with spark on time, attains maximum value, and shows a decreasing trend further, possibly due to the constant duty factor and decrease in flux density. A similar trend is also shown in the experimental results reported by Panda and Bhoi [25]. As the current increases, the peak of the curves shifts towards the right side indicating increase in MRR with current and spark on time simultaneously. This trend of variation, in effect, justifies the use of equivalent spark radius proposed in our model (see "Section 4.2," Eq. 4), which is a function of both discharge current as well as the spark on time.

Similar to MRR, the TWR also increases with the discharge duration until it reaches maximum value and then decreases possibly due to the constant duty factor and decrease in flux density (see Fig. 12). The trend of variation of TWR with spark on time is also demonstrated by the experimental results reported by Patel et al. [17]. There is very little tool wear with discharge duration more than 300 μs suggesting suitable conditions for finishing operation.

Figures 13 and 14 show that both the crater depth and crater radius increase with spark on time; the rate of increase, however, tapers off subsequently. A higher value of spark on time produces deeper and wider craters but causes reduction in MRR. Results reported in Table 4 (no. 3–4, 6–7, 11–12,

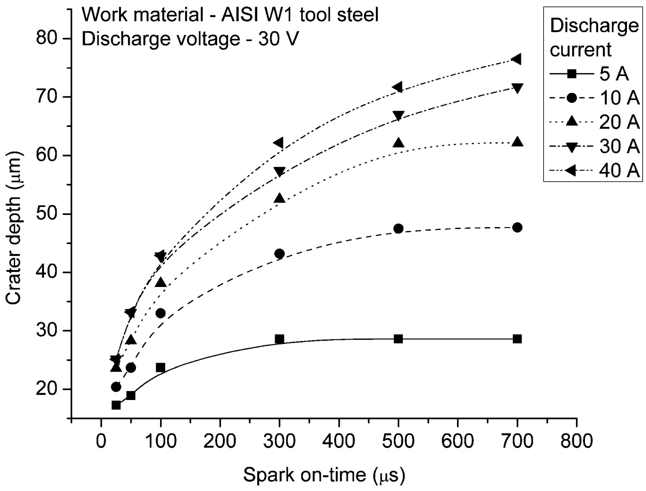

Fig. 13 Variation of crater depth with spark on time

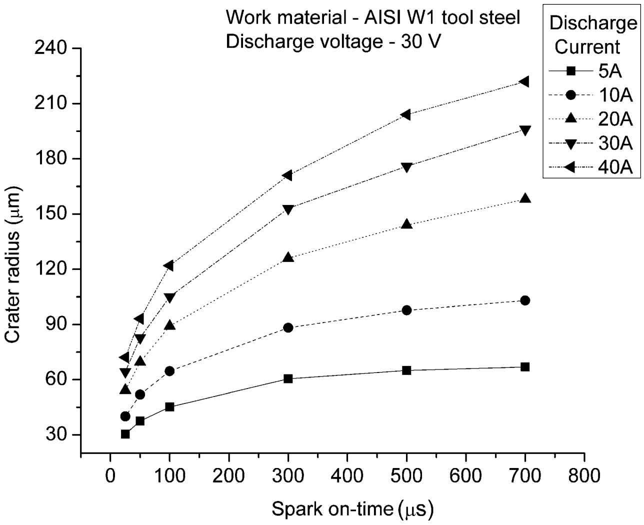

Fig. 14 Variation of crater radius with spark on time

and 14–15) clearly show this trend, viz. increase in the crater radius with spark on time, but with a significant reduction in MRR. Increase in crater radius and crater depth will cause increase in the material removed per pulse. However, for a constant duty factor, as the spark on time increases, the number of sparks per unit time decreases. This in turn will reduce the MRR. In addition, problems of arcing, ignition delays, and improper flushing of debris due to long discharge duration will further contribute to the reduction in MRR.

5.4 Effect of discharge voltage

Discharge voltage is an important process parameter which governs the heat flux applied on the cathode surface. Table 4 shows the variation of MRR and TWR with discharge voltage for various values of discharge current and spark on time. MRR and TWR are both seen to increase with the discharge voltage. Higher values of discharge voltage increase the flux density producing higher local temperatures both at anode and cathode surfaces. This enhances the material removal as well as the tool wear. Higher values of discharge voltages are recommended for roughing application.

From the above results, it is seen that the performance measures of EDM process are influenced by four interacting process parameters, viz. discharge current, discharge duration, discharge voltage, and duty factor. A complex nonlinear relationship seems to exist between these process parameters and process performance measures such as MRR, TWR, and crater depth. In the absence of a good process model, it is quite difficult to select the optimum process parameters for specific application of EDM process, viz. roughing or finishing. Traditionally, the selection of the most favorable EDM process parameters is based on trade literature, shop experience which might lead to subjectivity and inconsistent machining performance [1, 3, 4].

Neural networks are known to have excellent function mapping capabilities even from incomplete and noisy data [38]. It is, therefore, thought appropriate to develop an ANN-based comprehensive EDM process model using the results obtained from the numerical (FEM) model developed.

6 ANN-based process model for EDM

A neural network is a massive parallel-distributed processor that has a natural propensity to extract patterns from input data and learn complex relationships between sets of input and output data for function approximation. Capabilities of ANN are governed by characteristics of neurons, network architecture, and training algorithms [39].

The present work was aimed at establishment of correlation between input process parameters such as current, discharge voltage, discharge duration, and duty factor with process responses viz. MRR, TWR, and crater dimensions using suitable neural network algorithm. Literature reports several attempts to model EDM process using ANN configurations like BPNNs or RBFN. BPNNs (also called multilayer perceptrons, MLPs) are one of the most commonly used artificial neural networks which have been successfully used for a wide variety of applications, such as speech or voice recognition, image pattern recognition, medical diagnosis, automatic controls, etc. [39]. RBFN is the alternative supervised learning network architecture to the popular MLPs. It can be represented with radially symmetric hidden neurons. The topology of the RBFN is similar to the three-layered MLP but the characteristics of the hidden neurons are different. RBFN requires more neurons than the standard feed-forward backpropagation network but comparatively takes much less time to learn and is simpler to configure [40, 41]. For selecting an appropriate ANN configuration for our EDM process modeling problem, both BPNN and RBFN configurations with supervised learning paradigm were extensively tried out.

Initially, multi-input–multi-output (4–N–4) RBFN configuration was tried out due to its simplicity in design and faster convergence characteristics. The RBFN network was trained with the data generated from numerical (FEM) simulations by varying the spread factor and the number of neurons in the hidden layer. The network was trained with 260 datasets and was tested with 13 (unseen) datasets. The spread factor was varied within 0.1 to 0.4 [42]. The network with 250 hidden neurons and a spread factor of 0.14 provided better results. This best possible network, however, gave very poor prediction performance (prediction error of the order of 50–200%). The poor generalization capability of the RBFN network for these data might be due to insufficient training data and local nature of fitting [45]. In comparison, BPNN configuration with a fast learning algorithm, viz. scaled conjugate gradient (SCG) gave much superior results for our problem. The details regarding the development of BPNN-based process model, viz. network architecture, training, testing, and the selection of suitable ANN architecture for our problem, are presented in the next section.

6.1 Development of BPNN-based process model

BPNN is a multilayered feed-forward neural network which is trained using the supervised learning philosophy using backpropagation algorithm. Basic components of BPNN network are the neurons, network architecture, and its algorithm. The neuron is an information-processing element which modifies the received information by using a nonlinear activation function and further passes it to the next layer. The network consists of an input layer, a variable number of hidden layers each containing number of hidden nodes/neurons, and an output layer [39]. The architecture proposed in this work is shown in Fig. 15.

The input layer receives the information from an external source (data), which is subsequently modified by the interconnection weights between it and the adjacent hidden layer. The sum of the modified signals is then operated upon by a suitable transfer function, and these activated values, in turn, become the starting signals for the next adjacent layer. In this way, the modified signal finally reaches the output layer where the deviations (errors) of the predicted outputs from the desired outputs are calculated. The input–output patterns are sequentially presented to the network for training and the various interconnections are adjusted using error backpropagation algorithm. The process is repeated iteratively until the mean square error falls below a prescribed limiting value [39].

$$\mathrm{MSE} = \frac{1}{P}\sum_{p=1}^{P}\sum_{k=1}^{M}\left(d_k^p - c_k^p\right)^2 \tag{6}$$

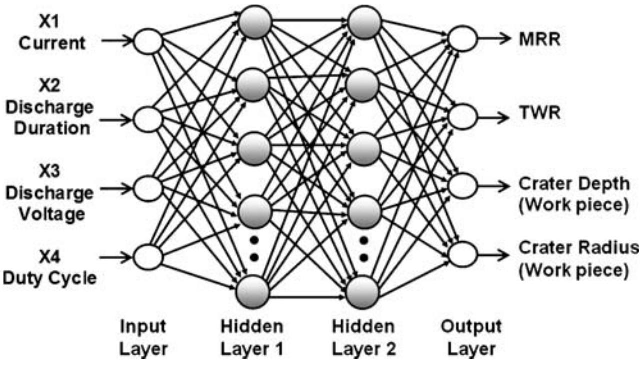

Fig. 15 Schematic of BPNN architecture

where P is the number of patterns; M is the number of nodes in the output layer; d_k^p is the desired output of the kth node of pth pattern, c_k^p is the calculated output of the kth node of pth pattern.

BPNN can be trained with many training algorithms such as gradient descent (GD), GD with momentum (GDA), Levenberg–Marquardt (LM), conjugate gradient (CG), SCG, etc. These training algorithms are employed to adjust the weights during training of the network. The GD algorithm is generally very slow because it requires small learning rates for stable learning [44]. The momentum variation (GDA) is usually faster than simple gradient descent since it allows higher learning rates while maintaining stability, but it is still too slow for many practical applications. As with linear networks, too large learning rate leads to unstable learning, while too small learning rate results in long training times. For nonlinear multilayer, it is further difficult to select the optimal value of learning rate. Normally, GD and GDA are used for incremental training of the networks [42].

LM and CG are comparatively faster training algorithms but they have limited applicability due to the need of large memory and slower convergence. To overcome some of the disadvantages of the above training algorithms, Moller [44] developed an SCG using model search region approach of LM algorithm and CG algorithm for fast supervised learning. Incorporation of the “adaptive learning” feature (optimization of learning rate in each iteration) and no-line search technique makes this algorithm easy and simple to configure and computationally inexpensive. The BPNN architecture can be configured just by selecting the number of hidden layers and optimal number of neurons in hidden layers for best possible generalization of the network. Hence, in this work, scaled conjugate gradient algorithm is used for the training of the network.

Selection of number of hidden layers and number of neurons in the hidden layers are important parameters in the optimal BPNN configuration. Too few neurons in the hidden layer can lead to underfitting while too many neurons can contribute to overfitting, in which all training points are well fit, but the fitting curve takes wild oscillations between these points. No standard guidelines are available for selecting the number of neurons and number of hidden layers. These can be selected by using trial and error method and examining the generalization capability of the network. The various network and training parameters used for training and testing the BPNN network are listed in Table 5.

6.1.1 Network training and testing data

In this work, thermophysical analysis of single-spark EDM process using FEM has been carried out (“Section 4”) to

Table 5 Network and training parameters

Parameter	Description/value
Number of hidden layers	1, 2
Number of neurons per hidden layer	Single hidden layer architecture—4 to 45
	Two hidden layer architecture—4 to 30
Transfer functions	Tangent sigmoid for hidden layers
	Log sigmoid for output layer
Training algorithm	Scaled conjugate gradient [44]
Performance function	Mean squared error
Number of epochs	10,000–12,000
MSE threshold (or goal)	1.00e−05

predict the shape of the crater cavity and to compute the material removal per pulse (MRP). For specified ranges of these input process parameters ("Section 5"), a total of 90 numerical experiments (simulations) for each work–tool material pair have been carried out to calculate the MRP values. The duty factor values ranging from 50% to 80% have been used to compute the MRR/TWR. Thus, a total of 270 (90×3) MRR/TWR values were estimated using the results of the single-spark analysis and the duty factor. In addition, three intermediate input–target pairs were chosen randomly to test the interpolation capability of the trained networks. The dataset thus comprised of 273 input–target pairs. This dataset was divided into a training set (260 input–target pairs) and a testing set of (13 input–target pairs). Table 6 shows total 13 datasets of typical machining conditions used for testing the various ANN architectures. Normalization of input vectors and target values was carried out to get good convergence. The training and testing datasets were normalized as below [25]

$$x_n = 0.1 + \left(\frac{x}{1.2 \times x_{\max}}\right) \quad (7)$$

where x_n is the normalized value of variable x; $x_{\max}$ is the maximum value of x in total datasets.

6.1.2 Training and testing

Extensive training and testing of different network architectures for the chosen training set was carried out by varying the number of hidden layers and number of neurons in the hidden layer. Testing of the trained network was carried out in two phases. Firstly, it was tested with seen input datasets (training set). In the second phase of the testing, the network was tested with unseen input datasets (testing set). Error

Table 6 Datasets for testing the ANN architectures

Sr. no.	Input process parameters				Output performance parameters			
	Duty factor (%)	Current (A)	Spark on time (μs)	Discharge voltage (V)	MRR (mm^3/min)	TWR (mm^3/min)	Crater depth (μm)	Crater radius (μm)
1	50	20	50	30	161.4	11.2	29.9	69.6
2	50	20	100	40	212.7	7.7	42.8	95.5
3	65	5	25	50	80.8	8.1	22.0	34.4
4	65	10	100	40	131.4	0.9	36.2	70.3
5	65	30	25	30	296.4	79.1	25.1	64.3
6	80	5	50	50	97.0	2.6	26.7	44.2
7	80	20	300	50	428.8	8.1	67.0	147.0
8	80	30	100	40	523.2	71.8	46.1	115.0
9	80	40	25	30	485.8	153.6	25.1	72.1
10	80	40	700	50	884.6	6.9	100.3	266.0
11	60	25	225	45	358.3	12.5	60.6	144.0
12	70	25	75	35	331.7	34.3	37.8	91.3
13	60	35	80	35	388.7	59.3	38.9	109.0

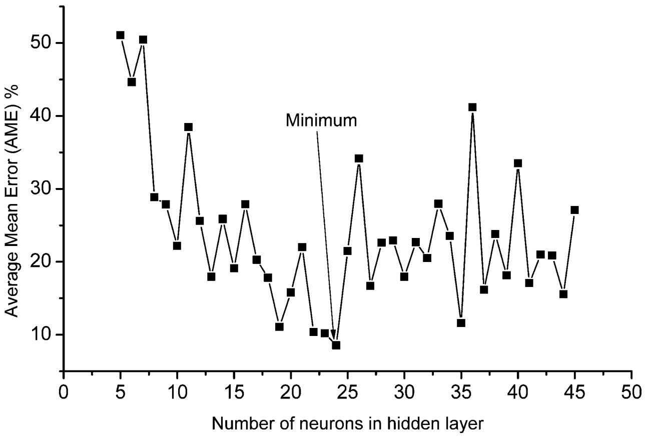

Fig. 16 Selection of number of nodes for 4–N–4 BPNN architecture

value is the numerical difference between the actual value of the output performance parameter (numerical simulations using FEM) and the value predicted by the trained network. The prediction error is defined as

$$\text{prediction error (PE)\%} = \left(\frac{\text{ideal value (FEM)} - \text{predicted value (ANN)}}{\text{ideal value (FEM)}}\right) \times 100 \tag{8}$$

Then, the mean error (ME) of the testing datasets for each of the output performance parameters (MRR, TWR, crater depth, and crater radius) was calculated.

$$\mathrm{ME} = \frac{\sum_{i=1}^{n} \mathrm{PE}}{n} \tag{9}$$

where n=13 is the number of datasets used for testing.

The average mean error (AME) of all the output performance parameters was then evaluated. It was further used for selecting the optimal network configuration.

$$\mathrm{AME} = \frac{\mathrm{ME}_{\mathrm{MRR}} + \mathrm{ME}_{\mathrm{TWR}} + \mathrm{ME}_{\mathrm{crater-depth}} + \mathrm{ME}_{\mathrm{crater-radius}}}{4} \tag{10}$$

BPNN (MLPs) often have one or more hidden layers which allow the network to learn nonlinear relationships between input and output vectors. In our problem, two BPNN architectures were tried out, viz. single-layered (4–N–4) and two-layered (4–N1–N2–4). Extensive numerical experimentations were carried out using MATLAB™ NN Toolbox [42] to select the optimal network architecture. The details are as follows.

6.1.3 The 4–N–4 architecture

In this architecture, a single hidden layer was taken and the number of hidden neurons (*N*) was varied from five to 45. BPNN network simulations were carried out with the network parameters listed in Table 5. Figure 16 shows the variation of AME with the number of neurons in the hidden layer. BPNN network with 24 neurons gave minimum AME. Figure 17 shows the typical convergence graph during the training of the BPNN network with 24 hidden neurons. The network got trained well by 7,000 epochs.

Table 7 shows the prediction error of the 4–N–4 BPNN architecture with 24 hidden neurons for all the four output performance parameters. It is seen that the network generalized well for predicting MRR, crater depth, and crater radius with prediction error within the range of 0.5–10% with the average accuracy of 2.43%. In comparison, the network provided poor generalization for the TWR with average prediction accuracy of 26.86%. It can be noted that only 62% of the testing datasets lie within a 15% error bound. This might be due to the nonlinear and complex relationship variation of TWR with input process parameters. To improve upon the generalization capability of the network for all four output process parameters, it was decided to try the two-layer BPNN architecture of the type 4–N1–N2–4.

6.1.4 The 4–N1–N2–4 architecture

In this architecture, two hidden layers were employed to improve the generalization capability of the ANN model. The network parameters listed in Table 5 were used for training the networks. The number of neurons in both the hidden layers was sequentially varied from four to 30. A total of 729 network simulations were carried out for selecting the optimal network architecture. Figure 18 shows the convergence graph of 4–8–12–4 network during training. It can be noted that by adding one more layer to

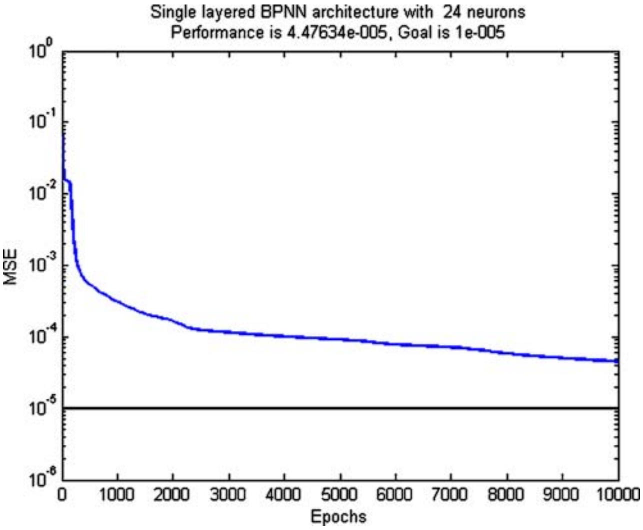

Fig. 17 Training of 4–24–4 BPNN network

Table 7 Testing of 4–N–4 BPNN architecture

Sr. no.	Input process parameters				Prediction error (%)			
	Duty factor (%)	Current (A)	Spark on time (µs)	Discharge voltage (V)	MRR	TWR	Crater depth	Crater radius
1	50	20	50	30	−0.6	7.5	−3.3	0.5
2	50	20	100	40	−1.4	−103.0	−2.5	−3.8
3	65	5	25	50	1.7	−26.3	0.7	0.3
4	65	10	100	40	1.6	−21.9	−3.3	−0.8
5	65	30	25	30	0.6	−1.8	4.1	2.9
6	80	5	50	50	−10.1	−12.2	−1.5	−1.5
7	80	20	300	50	−1.7	−12.7	0.9	−0.7
8	80	30	100	40	0.4	0.5	2.3	0.6
9	80	40	25	30	3.1	5.2	−1.8	−1.9
10	80	40	700	50	2.5	−124.8	2.9	1.5
11	60	25	225	45	−1.9	0.2	−2.1	−0.8
12	70	25	75	35	5.7	−19.4	6.4	2.9
13	60	35	80	35	2.7	−13.7	5.7	5.0

the single-layer architecture the network got trained properly by giving an error of 2.4828e−5 in 12,000 epochs.

Table 8 shows some typical candidate network architectures among the total of 729 networks which were experimented upon for the selection of optimal network architecture based on minimum AME criteria. It is seen that the architecture with eight and 12 neurons in the first and second hidden layers, respectively (4–8–12–4), gives minimum AME of 5.45%. The network 4–8–12–4 shows excellent average prediction accuracy of 1.49% for MRR, crater depth, and crater radius. For TWR, the 4–8–12–4 architecture generalized much better compared to single-layer architecture by reducing the ME from 26.86% to 17.34%.

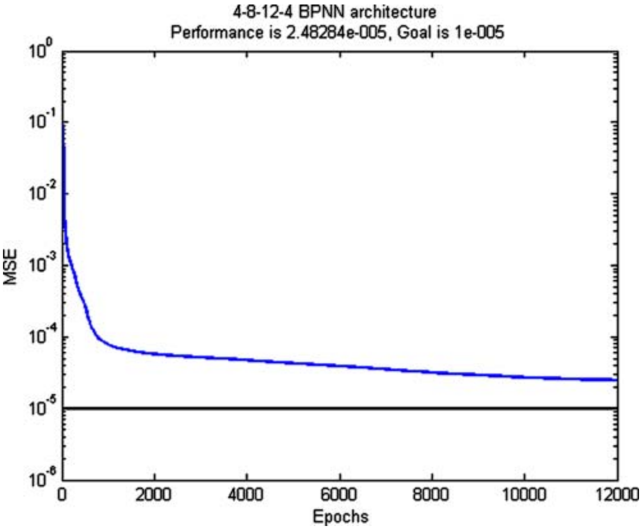

Fig. 18 Training of 4–8–12–4 BPNN network

Table 9 shows the comparison of the FEM results with the results predicted using 4–8–12–4 BPNN network for typical machining conditions (unseen dataset). The results show excellent prediction accuracy of the BPNN-based process model developed for the prediction of MRR (−0.03 to −3.53%), crater depth, and crater radius (around 1.47%). For TWR, it shows an acceptable average prediction accuracy of 17.34%. It is observed that a total of 77% of the total testing datasets lie within 15% of error bound. It can be concluded that the two-layer architecture (4–8–12–4) enhanced the generalization capability of BPNN architecture by better capturing the nonlinear and complex relationship of all four output performance parameters with the input process parameters.

7 Conclusions

An intelligent approach for the modeling and simulation of die-sinking EDM process is developed using FEM and ANN. Comprehensive thermal analysis of EDM process was carried out using two-dimensional axisymmetric nonlinear transient FEM model. The results obtained from our numerical model were compared with earlier analytical models and the published experimental data. It was found that the results predicted by our model are closer to experimental results compared to all the reported analytical models. Incorporation of factors such as the Gaussian distribution of heat flux and EDM spark radius as a function of discharge energy and discharge duration probably made our model closer to actual process conditions, thus improving prediction accuracy.

Table 8 Candidate 4–N1–N2–4 network architectures

Sr. no.	Number of neurons in first hidden layer (N1)	Number of neurons in first hidden layer (N2)	Mean error of testing datasets % (on actual values)				AME%
			MRR	TWR	Crater depth	Crater radius	
1	6	28	1.86	24.21	1.59	0.8	7.12
2	7	25	1.78	26.99	2.1	1.04	7.98
3	7	30	2.01	27.84	1.85	1.22	8.23
4	8	12	1.53	17.34	1.78	1.16	5.45
5	8	20	1.39	20.41	2.08	1.13	6.25
6	8	30	1.66	22.01	1.91	1.02	6.65
7	9	18	2.14	17.92	2.11	1.31	5.87
8	9	25	5.4	19.93	4.7	5.19	8.8
9	10	26	2.8	22.65	1.53	1.41	7.1
10	10	30	4.1	30.47	2.28	2.05	9.73
11	11	15	2.64	28.49	2.45	2.36	8.98
12	11	29	3.84	21.05	3.7	2.04	7.66
13	12	14	2.94	27.14	1.78	1.77	8.41
14	12	16	2.72	28.45	2.04	1.36	8.64
15	12	18	2.22	17.14	2.8	1.89	6.01
16	12	19	2.13	22.37	2.29	2	7.2
17	13	9	1.72	18.93	2.85	1.68	6.3
18	13	10	1.5	26.75	2.03	1.54	7.95
19	13	23	2.18	20.36	2.01	2.24	6.7
20	16	10	2.8	30.63	1.61	1.45	9.12
21	17	23	3.67	23.84	5.14	3.76	9.1
22	19	22	6.07	22.54	3.99	3.63	9.06
23	20	19	4.7	25.45	3.86	3.75	9.44
24	26	12	3.06	27.86	3.58	3	9.37
25	26	13	3.5	23.59	3.53	3.65	8.57

Table 9 Testing of 4–N1–N2–4 BPNN architecture

Sr. no.	Input process parameters				Prediction error (%)			
	Duty factor (%)	Current (A)	Spark on time (μs)	Discharge voltage (V)	MRR	TWR	Crater depth	Crater radius
1	50	20	50	30	−1.35	−10.99	−0.97	0.96
2	50	20	100	40	−1.16	−79.67	−0.53	0.73
3	65	5	25	50	2.48	0.77	−0.36	2.49
4	65	10	100	40	0.56	8.35	−2.58	−0.53
5	65	30	25	30	−0.03	5.67	1.77	0.94
6	80	5	50	50	−0.80	−44.27	−1.18	3.61
7	80	20	300	50	−3.53	−6.46	−0.32	−1.24
8	80	30	100	40	0.45	3.70	−0.02	0.02
9	80	40	25	30	1.66	1.79	−1.50	1.35
10	80	40	700	50	2.44	−41.28	3.76	0.74
11	60	25	225	45	−3.07	−14.39	−0.88	0.05
12	70	25	75	35	0.08	6.04	−2.14	−1.26
13	60	35	80	35	−2.26	2.04	−7.15	−1.19

Important process parameters were identified and their effects on performance parameters were extensively studied. Using results from the numerical simulations of our model, BPNN-based process model was developed and optimized for the prediction of material removal, tool wear, and crater dimensions. Extensive numerical simulations were carried out to select the optimal BPNN network architecture by varying the number of hidden layers and number of neurons in the hidden layers. Optimal network architecture 4–8–12–4 was found to give very good prediction accuracies for MRR (1.53%), crater depth (1.78%), and crater radius (1.16%) and a reasonable one for TWR (17.34%).

The ANN-based process model can be used to select optimum process conditions to improve EDM process productivity and finishing capability. This will be the focus of our future work.

References

1. Ho KH, Newman ST (2003) State of the art in electrical discharge machining (EDM). Int J Mach Tools Manuf 43:1287–1300. doi:10.1016/S0890-6955(03)00162-7
2. Descoeudres A (2006) Characterization of electrical discharge machining plasmas. Ph.D. Thesis. EPFL Lausanne
3. Kunieda M, Lauwers B, Rajurkar KP, Schumacher BM (2005) Advancing EDM through fundamental insight into the process. CIRP Ann 54(2):599–622. doi:10.1016/S0007-8506(07)60020-1
4. Abbas NM, Solomon DG, Bahari Md F (2007) A review on current research trends in electrical discharge machining (EDM). Int J Mach Tools Manuf 47:1214–1228. doi:10.1016/j.ijmachtools.2006.08.026
5. Singh A, Ghosh A (1999) Thermo-electric model of material removal during electric discharge machining. Int J Mach Tools Manuf 39(4):669–682. doi:10.1016/S0890-6955(98)00047-9
6. Snoeys R, Van Dijck FS (1971) Investigation of electro discharge machining operations by means of thermo-mathematical model. CIRP Ann 20(1):35–37
7. Snoeys R, Van Dijck FS, Peters J (1972) Plasma channel diameter growth affects stock removal in EDM. CIRP Ann 21(1):39–40
8. Van Dijck FS, Dutre WL (1974) Heat conduction model for the calculation of the volume of molten metal in electric discharges. J Phys D Appl Phys 7(6):899–910. doi:10.1088/0022-3727/7/6/316
9. Erden A, Kaftanoglu B (1981) Heat transfer modeling of electric discharge machining. In: Proceedings of the 21st International Machine Tool Design and Research Conference, Swansea Wales Univ. Coll. of Swansea, Dept. of Mech. Eng., Wales in Assoc. with Macmillan Press, Ltd. London, UK, pp. 351–358
10. Beck JV (1981a) Transient temperatures in a semi-infinite cylinder heated by a disk heat source. Int J Heat Mass Transfer 24(10):1631–1640. doi:10.1016/0017-9310(81)90071-5
11. Beck JV (1981b) Large time solutions for temperatures in a semi-infinite body with a disk heat source. Int J Heat Mass Transfer 24 (1):155–164. doi:10.1016/0017-9310(81)90104-6
12. Jilani ST, Pandey PC (1982) Analysis and modelling of EDM parameters. Precis Eng 4(4):215–221. doi:10.1016/0141-6359(82)90011-3
13. Jilani ST, Pandey PC (1983) Analysis of surface erosion in electrical discharge machining. J Wear 84(3):275–284. doi:10.1016/0043-1648(83)90269-7
14. Pandit SM, Rajurkar KP (1983) A stochastic approach to thermal modeling applied to electro discharge machining. ASME Trans J Heat Transf 105:555–561
15. Pandey PC, Jilani ST (1986) Plasma channel growth and the resolidified layer in EDM. Precis Eng 8(2):104–110. doi:10.1016/0141-6359(86)90093-0
16. DiBitonto DD, Eubank PT, Patel MR, Barrufet MA (1989) Theoretical models of the electrical discharge machining process - I A simple cathode erosion model. J Appl Phys 66(9):4095–4103. doi:10.1063/1.343994
17. Patel MR, Barrufet MA, Eubank PT, DiBitonto DD (1989) Theoretical models of the electrical discharge machining process. II. The anode erosion model. J Appl Phys 66(9):4104–4111. doi:10.1063/1.343995
18. Salah NB, Ghanem F, Atig KB (2006) Numerical study of thermal aspects of electric discharge machining process. Int J Mach Tools Manuf 46(7–8):908–911. doi:10.1016/j.ijmachtools.2005.04.022
19. Marafona J, Chousal JG (2006) A finite element model of EDM based on the Joule effect. Int J Mach Tools Manuf 46(6):595–602. doi:10.1016/j.ijmachtools.2005.07.017
20. Yeo SH, Kurnia W, Tan PC (2007) Critical assessment and numerical comparison of electro-thermal models in EDM. J Mater Process Technol 203:241–251. doi:10.1016/j.jmatprotec.2007.10.026
21. Tsai KM, Wang PJ (2001) Comparison of neural network models on material removal rate in EDM. J Mater Process Technol 117:111–124. doi:10.1016/S0924-0136(01)01146-3
22. Wang K, Gelgele HL, Wang Y, Yuan Q, Fang M (2003) A hybrid intelligent method for modeling the EDM process. Int J Mach Tools Manuf 43:995–999. doi:10.1016/S0890-6955(03)00102-0
23. Su JC, Kao JY, Tarng YS (2004) Optimisation of the electrical discharge machining process using a GA-based neural network. Int J Adv Manuf Technol 24:81–90
24. Amalnik MS, Farzad M (2005) Neural network radial based function (RBF) approach in predicting of material removal rate and surface roughness in electrical discharge machining, In: Proceedings of systems of designing, technological preparation of manufacture and management of stages of life cycle of industrial product CAD/CAM/PDM-2005, http://lab18.ipu.rssi.ru/projects/conf2005/Accessed 19th July 2007
25. Panda DK, Bhoi RJ (2005) Artificial neural network prediction of material removal rate in EDM. Mater Manuf Process 20:645–672. doi:10.1081/AMP-200055033
26. Mandal D, Pal SK, Saha P (2007) Modeling of EDM using BPNN and multi-objective optimization using non dominating sorting algorithm—II. J Mater Process Technol 186:154–162. doi:10.1016/j.jmatprotec.2006.12.030
27. Das S, Klotz M, Klocke F (2003) EDM simulation: finite element-based calculation of deformation, microstructure and residual stresses. J Mater Process Technol 142:434–451. doi:10.1016/S0924-0136(03)00624-1
28. Kansal HK, Singh S, Kumar P (2007) Numerical simulation of powder mixed electric discharge machining (PMEDM) using finite element method. Math Comp Modelling 47:1217–1237. doi:10.1016/j.mcm.2007.05.016
29. Erden A (1983) Effect of materials on the mechanism of electric discharge machining. Trans ASME 105:132–138
30. Shankar P, Jain VK, Sundarajan T (1997) Analysis of spark profiles during EDM process. Machining Sci Tech 1(2):195–217. doi:10.1080/10940349708945647
31. Ikai T, Hashigushi K (1995) Heat input for crater formation in EDM. In: Proceedings of International Symposium for Electro Machining-ISEM XI, EPFL, Lausanne, Switzerland, pp 163–170
32. Yeo SH, Kurnia W, Tan PC (2007) Electro-thermal modeling of anode and cathode in micro-EDM. J Phys D Appl Phys 40:2513–2521. doi:10.1088/0022-3727/40/8/015

33. ANSYS manuals version 10.0, ANSYS TM Inc., USA
34. Dong KK (2004) Electrical discharge machining mechanism analysis and simulation using finite element method. Ph. D. Thesis. The Graduate School of Yonsei University, Seoul, Korea
35. Schulze HP, Herms R, Juhr H, Schactzing W, Wollenberg G (2004) Comparison of measured and simulated crater morphology for EDM. J Mater Process Technol 149:319–322. doi:10.1016/j.jmatprotec.2004.02.016
36. Efunda (2007) http://www.efunda.com. Accessed 02nd July 2007
37. Chen Y, Mahdivian SM (2000) Analysis of electro-discharge machining process and its comparison with experiments. J Mater Process Technol 104:150–157. doi:10.1016/S0924-0136(00)00531-8
38. Ramasawmy H, Blunt L (2004) Effect of EDM process parameters on 3D surface topography. J Mater Process Technol 148:155–164. doi:10.1016/S0924-0136(03)00652-6
39. Haykin S (2005) Neural networks a comprehensive foundation. Pearson Education Inc, Singapore
40. Bi TS, Ni YX, Shen CM, Wu FF, Yang QX (2000) A novel radial basis function neural network for fault section estimation in transmission network. In: Proceedings of the 5th International Conference on Advances in Power System Control, Operation and Management, APSCOM 2000, Hong Kong, pp 259–263
41. Chen S, Cowan CFN, Grant PM (1991) Orthogonal least squares learning algorithm for radial basis function networks. IEEE Trans Neural Netw 2:302–309. doi:10.1109/72.80341
42. MATLAB version 7.0 Neural Network Tool Box, The MathWorks TM Inc., USA
43. Machining Data Handbook V2 (1981). Machiniability data center, Metcut Research Associates Inc., USA
44. Moller MF (1993) A scale conjugate gradient algorithm for fast supervised learning. Neural Netw 6:525–533. doi:10.1016/S0893-6080(05)80056-5
45. Pal SK, Garg S, Chakraborty D (2007) Evaluation of the performance of back propagation and radial basis function neural networks in predicting the drill flank wear. Neural Comput Appl 16:407–417. doi:10.1007/s00521-006-0065-7